

Observation of laser-assisted electron scattering in superfluid helium

Leonhard Treiber¹, Bernhard Thaler¹, Pascal Heim¹, Michael Stadlhofer¹, Markus Kitzler-Zeiler²,
and Markus Koch^{*1}

¹Graz University of Technology, Institute of Experimental Physics, Petersgasse 16, 8010 Graz,
Austria

²Technische Universität Wien, Photonics Institute, Gusshausstrasse 27-29, 1040 Vienna, Austria

Abstract

Laser-assisted electron scattering (LAES), a light–matter interaction process that facilitates energy transfer between strong light fields and free electrons, has so far been observed only in gas phase. Here we report on the observation of LAES at condensed phase particle densities, for which we create nano-structured systems consisting of a single atom or molecule surrounded by a superfluid He shell of variable thickness (32–340 Å). We observe that free electrons, generated by femtosecond strong-field ionization of the core particle, can gain several tens of photon energies due to multiple LAES processes within the liquid He shell. Supported by 3D scattering simulations, these results provide the first insight into the interplay of LAES energy gain/loss and dissipative electron movement in a liquid. Our results reveal that LAES could significantly increase the temporal resolution of ultrafast electron microscopy, potentially to the attosecond regime.

*corresponding author: markus.koch@tugraz.at

Introduction

The investigation of atomic-scale processes with high spatio-temporal resolution is key to the understanding and development of materials. While pulsed light sources have been developed to provide attosecond temporal resolution [1], the diffraction limit of light waves prohibits the improvement of the spatial resolution below the ten-nanometer range. Electron probes, in contrast, allow for subatomic spatial resolution due to their picometer deBroglie wavelength, and can, in principle, achieve the temporal resolution of light pulses. Time-domain shaping of electron pulses is based on the transfer of energy between electromagnetic radiation and free electrons, which is manifested in various phenomena, such as bremsstrahlung, Smith-Purcell radiation [2], Cerenkov radiation [3], or Compton scattering [4]. Electron-photon coupling is furthermore key to the development of novel light sources like free electron lasers [5] or high-harmonic generation [6], and to ultrafast structural probing like high-harmonic spectroscopy [7] or laser-induced electron diffraction [8]. While few- and sub-femtosecond electron pulses [9, 10] and pulse trains [11, 12] could be generated through light-field manipulation, the time resolution achievable with these electron pulses suffers from velocity dispersion and Coulomb repulsion [10]. Consequently, spatial separation of pulse shaping and structural probing in ultrafast electron microscopy (UEM) setups [13, 14, 15, 16, 17, 18] leads to broadening of electron pulses during delivery to the sample, limiting the temporal resolution currently to about 80 fs [19].

LAES is a light-matter interaction process that holds promise to increase the temporal resolution of electron probes by combining velocity modulation and structural probing within the investigated sample. In LAES, free electrons that scatter off neutral atoms or molecules in presence of a strong laser field, can increase (inverse bremsstrahlung) or decrease (stimulated bremsstrahlung) their kinetic energy by multiples of the photon energy ($\pm n\hbar\omega$) [20, 21, 22]. Structural information of the scattering object is encoded in the angular distribution of the accelerated/decelerated electrons [23, 20]. Importantly, the energy modulation only takes place during the time window in which the short laser pulse overlaps with part of the much longer electron pulse within the sample. LAES can thus be viewed as an optical gating technique that allows to record scattering-snapshots at precisely defined times. The capability of LAES to analyze structural dynamics with subparticle spatial resolution (~ 1 pm) at timescales of electron dynamics (< 10 fs) was recently demonstrated in the gas-phase [23, 20]. However, in contrast to other strong-field phenomena [24], LAES has evaded observation in the condensed phase so far, so that its potential for advancing the time resolution of structural probing through UEM and other techniques remains unexplored.

Here, we demonstrate that LAES can be observed at condensed phase particle densities of $2 \cdot 10^{22} \text{ cm}^{-3}$, for which we create core-shell nanostructures, consisting of a single atom/molecule located inside a superfluid He droplet (He_N) [25, 26]. This system provides three unique advantages: First, the droplet size and thus the LAES interaction shell thickness underlies a well defined distribution, the mean of which can be varied with Angstrom resolution [25]. Second, the high strong-field ionization threshold of He [27] enables high laser intensities to increase the LAES probability without solvent ionization. Third, energy dissipation of electrons propagating inside He_N is very low [28]. We have chosen the experimental conditions to work in the multiple scattering regime in order to characterize the interplay of LAES acceleration/deceleration and dissipative electron movement within the He shell; as a consequence, our experiment does not provide information about the electron angular distribution.

Results

Observation of multiple LAES events

To measure the energy gain of electrons through LAES within the liquid He shell, we perform strong-field photoionization with femtosecond laser pulses and compare two photoelectron spectra that are recorded under the same laser pulse conditions: First, the above threshold ionization (ATI) spectrum of a bare, gas-phase atom/molecule and, second, the LAES spectrum obtained with the same atom/molecule embedded inside a He_N . The He droplets, which have a radius of a few nanometer, are created by supersonic expansion of He gas through a cryogenic nozzle and loaded with single dopant atoms or molecules through the pickup technique [25, 26], as described in the Methods section below. Figures 1a-c show the two types of spectra for three species: Indium (In) atoms, xenon (Xe) atoms, and acetone (AC) molecules. For all three species, the LAES spectrum shows significantly higher electron energies than the ATI spectrum, and both types of spectra—ATI and LAES—show equidistant signal modulations with a peak distance of 1.55 eV, corresponding to the central laser wavelength of 800 nm (1.55 eV photon energy). Closer inspection of the area-normalized spectra shows that, in addition to the higher energies of the LAES spectrum, the ATI signal exceeds the LAES signal at low energies up to $\sim 5 \text{ eV}$, indicating a shift of the electron energy distribution towards higher kinetic energies due to the presence of the He shell. The energy increase of the fastest electrons exceeds 20 eV in all three cases, which is far beyond the $10 U_P$ energy gain limit for a single scattering event according to the strong-field Kroll-Watson approximation [30] (U_P is the ponderomotive energy, see parameters

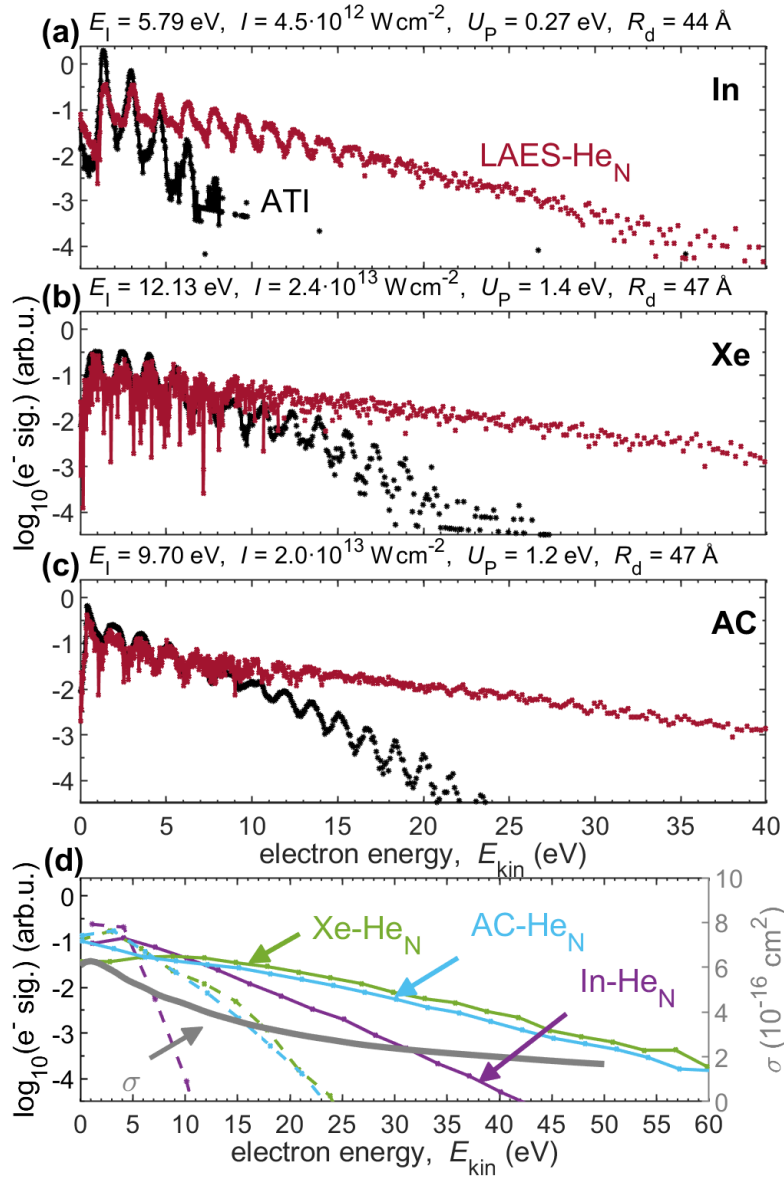


Figure 1: Comparison of electron spectra obtained by strong-field ionization with 800 nm light (1.55 eV photon energy) of different species in gas-phase (ATI spectra, black) and inside He_N (LAES spectra, red): (a) In atoms, (b) Xe atoms, (c) acetone (AC) molecules. The spectra are area-normalized in order to account for the reduced ionization energy inside a He_N [28]. Above each plot the values of the ionization energy, E_I , laser intensity, I , ponderomotive potential, U_P , and droplet radius, R_d , are listed. (d) ATI spectra (dashed lines) and LAES spectra (solid lines) as in a-c but with 3 eV binning (left ordinate), and cross section for total elastic electron scattering of electrons and He (gray line, right ordinate) [29].

above Figures 1a-c). Thus, a significant fraction of the electrons must encounter multiple LAES events within the liquid He shell.

In order to investigate the influence of the dopant species that serves as electron source through strong-field ionization, we compare the In, Xe and AC spectra (Figures 1a-c). We use a higher laser intensity I for Xe and AC due to the higher ionization energy E_I , compared to In, which is reflected by ATI spectra that extend to higher energies. Smoothed LAES and ATI spectra are compared in Figure 1d. The similarity of the Xe and AC spectra, for which a very similar laser intensity was used, indicates that the species from which the electrons originate has very little influence. Instead, the LAES energy gain is larger for Xe and AC (e.g., at a signal level of 10^{-3} : 25-30 eV gain), compared to In (20 eV gain), because of the higher laser intensities used for Xe and AC. These observations indicate that the laser intensity dictates the energy gain.

In addition to the LAES energy gain, insight into the dissipative electron movement within the liquid He shell can be obtained from the equidistant peak structure of the LAES spectra (Figures 1a-c). Kinetic energy of an electron can be dissipated to the He droplet through binary collisions with He atoms and through a collective excitation of the droplet. While elastic collision with a He atom reduces the electron kinetic energy by $\sim 0.06\%$ due to energy and momentum conservation, collective He_N excitations carry < 2 meV energy [26]. The pronounced contrast of the LAES peaks in Figure 1 thus demonstrates that energy dissipation plays a subordinate role compared to LAES energy gain for the relatively small droplets ($R_d \approx 45 \text{ \AA}$ radius) used in these measurements. Furthermore, the absence of a kink in the yield at or above 20 eV, the energy threshold of electronic He excitations [31], shows that inelastic interactions are insignificant, which is in agreement with the much lower cross section for inelastic as compared to elastic interaction [29].

Droplet size effects

We now investigate the influence of the He shell thickness on the LAES spectrum in order to deepen our insight into the interplay of light-induced energy gain/loss and dissipative energy losses. The He droplet approach allows to change the He shell thickness around the atom/molecule to be ionized by varying the droplet source temperature. Since LAES processes require electron-He scattering in presence of laser light, information about the electron transit time through the He shell can be gained from the droplet-size dependence of the LAES spectra. Figure 2a shows LAES spectra obtained with In atoms inside He droplets with radii from $R_d = 32 \text{ \AA}$ to $R_d = 340 \text{ \AA}$. The energy

gain continuously increases with the He shell thickness for the accessible range of droplet radii. The maximum kinetic energy doubles from 50 eV for the smallest droplets to 100 eV for the largest ones, compared to a maximum energy of the ATI spectrum of about 15 eV. This continuous increase provides a first indication that the transit time distribution, which is a result of stochastic electron trajectories, is comparable to the laser pulse duration, at least up to $R_d \approx 76 \text{ \AA}$.

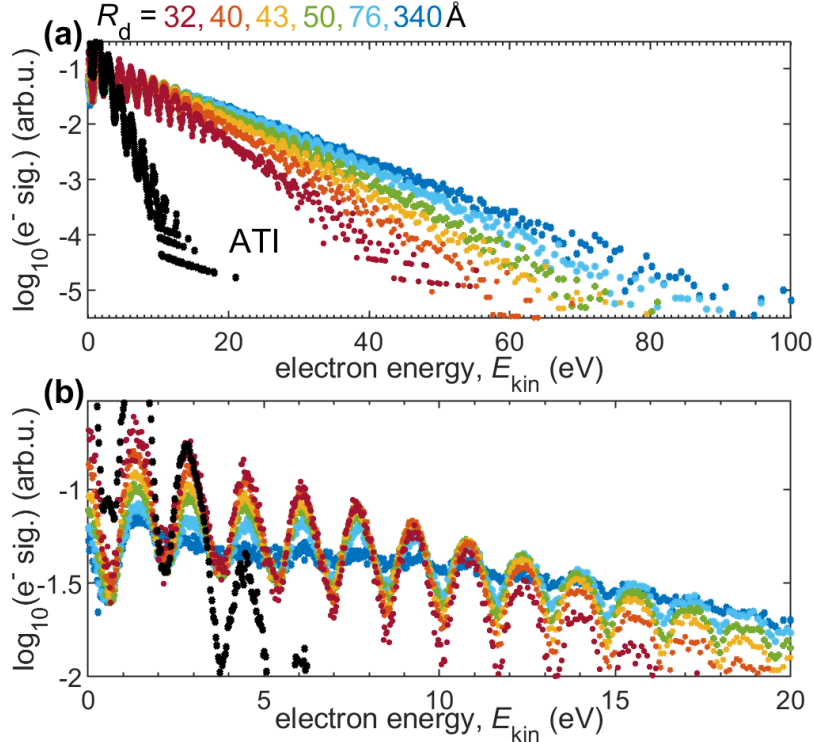


Figure 2: Dependence of LAES spectra on the droplet size, for droplet radii between $R_d = 32 \text{ \AA}$ and $R_d = 340 \text{ \AA}$ (R_d values are calculated from the mean values of the droplet size distributions [25]). The spectra are obtained with In atoms at $I = 1.1 \cdot 10^{13} \frac{\text{W}}{\text{cm}^2}$ and show a pronounced increase of the LAES energy gain with He shell thickness. Additionally, the gas-phase ATI spectrum is shown for comparison. The abrupt increase of the droplet radius to $R_d = 340 \text{ \AA}$ for the lowest droplet source temperature ($T_0 = 10 \text{ K}$) is due to the changing character of the supersonic expansion from sub- to supercritical in this temperature regime [25]. (b) Close-up of the low-energy region of (a).

While the LAES energy gain is restricted to the time window of the laser pulse, the electron dissipates energy as long as it propagates within the He droplet. Since the energy transfer in single collisions with He atoms is low, energy dissipation influences the modulation contrast of the LAES signal. A close-up of the LAES spectra in the low-energy region in Figure 2b allows to evaluate the dependence of this contrast on the droplet size. We find

that the contrast decreases steadily from the smallest droplets, where it equals the contrast of the gas-phase ATI peaks, until it vanishes completely for the largest droplets. We ascribe this blurring to energy dissipation of the electron within the He shell, which has increasing influence on the spectra for larger droplets. Despite the energy dissipation, the thickest He shell ($R_d = 340 \text{ \AA}$) supports the highest LAES energy gain, emphasizing the dominance of the light-driven electron energy modulation over dissipative energy loss.

3D scattering simulation

For further insight into the electron propagation through the He shell, we perform simple 3D elastic scattering simulations, without considering the light field. From these simulations we obtain estimations for the transit time and the number of electron–He scattering events. Figures 3a and b show the ratios of ejected electrons over time for $E_{\text{kin}} = 2 \text{ eV}$ and $E_{\text{kin}} = 10 \text{ eV}$, each for different droplet sizes. It can be seen that the probability for electron ejection within the time span of the laser pulse (25 fs) depends strongly on the droplet size, in particular for 2 eV electrons. This droplet size dependency is also reflected by the corresponding probability distributions of scattering events within 25 fs (insets of Figure 3a,b): The lower maximum of the double peak structure represents electrons that are ejected within 25 fs, while the upper maximum represents electrons that are inside the droplet after this time. We note that the actual time span for LAES is shorter than the pulse duration since the ionization is most likely around the pulse maximum, which might add to the uncertainty of the values discussed here, but does not influence the obtained trends.

The mean number of scattering events within 25 fs (Figure 3c) is predicted to increase with droplet size for all kinetic energies, eventually leveling off. Interestingly, in the biggest droplets 10 eV electrons experience more collisions than 2 eV electrons, because they propagate longer distances in larger droplets and thus undergo more collisions, despite their lower scattering cross section (Figure 1d).

Finally, we look into the dissipative electron movement and therefore consider 5 eV electrons and the scattering event distribution after ejection from the droplet (long interaction times, not restricted to 25 fs, Figure 3d). Comparing these distributions to the mean number of scattering events within the pulse duration in figure 3c, it is obvious, that for the biggest droplets, the majority of scattering events happen after the laser pulse.

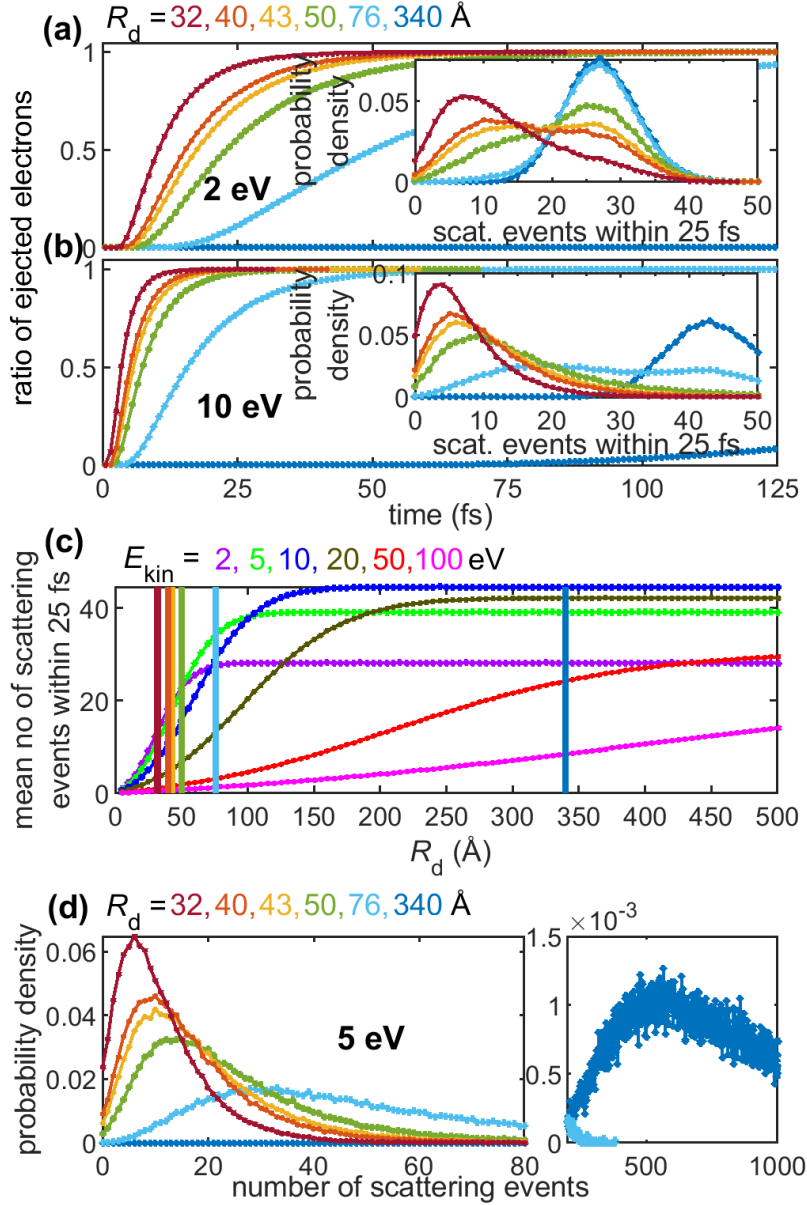


Figure 3: 3D simulation of electron trajectories inside a He droplet for different kinetic energies E_{kin} and different droplet radii R_d in similarity to Tulsy et al. [32]. An ensemble of $1 \cdot 10^5$ electrons is considered. **(a)** Probability that an $E_{\text{kin}} = 2$ eV electron has been ejected as function of time T for different R_d . Inset: Probability density of the number of scattering events within 25 fs for $E_{\text{kin}} = 2$ eV. **(b)** Same as (a) but for $E_{\text{kin}} = 10$ eV. **(c)** Mean number of scattering events within 25 fs [c.f., insets in (a) and (b)] as function of the droplet radius for $E_{\text{kin}} = 2, 5, 10, 20, 50, 100$ eV. Vertical lines indicate the R_d -values that are considered in (a) and (b). **(d)** Probability distribution of total scattering events, i.e., without temporal limit, for $E_{\text{kin}} = 5$ eV.

Discussion

Comparison of strong-field ionization spectra of atoms/molecules in gas phase and inside He droplets reveals that the presence of a nanometer-thick layer of superfluid He around the ionized particle leads to a significant increase of the electron kinetic energies. The following observations, in combination with predictions from 3D scattering simulations, lead us to the conclusion that the electron acceleration is due to multiple LAES processes within the He layer: (i) The energy gain strongly increases with droplet size (Figure 2). This behavior observed for strong-field ionization is in contrast to weak-field ionization inside He droplets, where the photoelectron spectrum is droplet-size independent because it is influenced only by the structure of the immediate environment of the dopant, the solvation shell [33]. In the current situation, the energy gain of the electron is related to the number of light-mediated binary electron–He-atom collisions at a distance from the remaining ion, which increases with growing droplet size. (ii) Comparison for three different species shows that the laser intensity has the strongest influence on the LAES energy gain, while the ionization energy plays a negligible role (Figure 1). This is explicable by an increased LAES probability due to increased photon flux. (iii) The upper limit of the energy gain by far exceeds the maximum light-field energy of $10 U_P$ that can be transferred to an electron in a single scattering event [30]. Multiple scattering events are in agreement with our simulations, which predict a broad distribution ranging up to several tens of scattering events even within the smallest droplets (Figure 3).

For the applicability of LAES in UEM, the interplay of LAES energy gain/loss and dissipative energy losses as a function of the thickness of the material is a crucial factor. We gain insight into the electron transit time through the He shell, as well as the number of dissipative electron–He-atom collisions, by comparing the droplet-size dependence of the LAES spectra to the scattering simulations. In the experiment we observe that the LAES energy gain increases continuously over the whole range of investigated droplet sizes ($R_d = 32 \text{ \AA}$ to $R_d = 340 \text{ \AA}$, Figure 2). This is in agreement with the simulations, which predict that the mean number of collisions within 25 fs, increases up to the largest droplets used in the experiment ($R_d = 340 \text{ \AA}$), most dominantly for higher electron energies. Consequently, the average transit time of the observed ensemble is on the order of the laser pulse duration. The LAES interaction time is determined by the droplet size in small droplets and by the laser pulse duration in large droplets (Figure 3).

Finally, we want to focus on the dissipative electron movement. Considering purely elastic scattering (Figure 3d), on

average, 5 eV electrons undergo 10 collisions inside the smallest droplets ($R_d = 32 \text{ \AA}$), resulting in an energy loss of 30 meV (0.06% energy loss per collision). Inside the largest droplets ($R_d = 340 \text{ \AA}$) they loose, on average, 2 eV after 830 elastic collisions. Comparing these values to the 1.55 eV distance of LAES peaks, the signal contrast is expected to be the same as that of the gas-phase ATI spectrum for the smallest droplets, while it can be expected to fully smear out for the largest droplets, in agreement with our measurements in Figure 2b. However, the simulated electron energy loss of 130 meV (45 collisions) for $R_d = 76 \text{ \AA}$, seems insufficient to explain the observed $\sim 50\%$ contrast reduction (around $E_{\text{kin}} = 5 \text{ eV}$) in figure 2b. This discrepancy points towards shortcomings of the simulation that are currently neglected: excitation of collective droplet modes [25, 26], transit-time increase due to Coulomb interaction between the ion core and the electron, or additional blurring of the LAES peaks due to sequential energy-gain–energy-loss processes with varying U_P . Nevertheless, the most important observation is that the largest He droplet (thickest He layer, $R_d = 340 \text{ \AA}$) yields the fastest electrons, proving that energy gain through multiple LAES processes effectively dominates energy dissipation for propagation distances of several tens of nanometers.

In conclusion, we have demonstrated that LAES can be observed with femtosecond laser pulses in the condensed phase at particle densities of $2 \cdot 10^{22} \text{ cm}^{-3}$. This demonstration shows that LAES can be used in the condensed phase to merge temporal selection via velocity modulation of electrons with ultrashort laser pulses (as demonstrated here), and structural analysis that can be extracted from the electron angular distributions [23, 20]. While it is encouraging that in superfluid He LAES energy modulation dominates energy dissipation of electrons, it will be important to investigate this ratio for other materials, which is enabled by the He droplet approach through the creation of core-shell systems [34, 35]. Photoionization of the core will allow to observe LAES-acceleration and energy dissipation within the shell material. Furthermore, extension to a pump-probe configuration with few-cycle pulses ($\sim 5 \text{ fs}$ duration) should enable the tracing of electron propagation within the target material. In view of UEM, our results suggest that LAES can increase the temporal resolution of electron probes through optical gating with ultrashort laser pulses.

Methods

Helium nanodroplet generation and particle pickup

We generate superfluid helium nanodroplets (He_N) in a supersonic expansion of high-purity He gas through a cooled nozzle (5 μm diameter, 40 bar stagnation pressure) into vacuum. Variation of the nozzle temperature between 10 and 20 K allows us to change the mean droplet size in the range of $\bar{N} = 3.0 \cdot 10^3 - 3.7 \cdot 10^6$ He atoms per droplet [25], corresponding to a droplet radius of $R_d = 32 - 340 \text{ \AA}$. After formation, evaporative cooling results in superfluid droplets at a temperature of about 0.4 K. We load the droplets with single atoms or molecules by passing them through a resistively heated pickup oven (In), or a gas pickup cell (Xe, acetone). While pickup conditions are optimized for single atom/molecule pickup, we found that the generation of dimers and larger complexes has negligible effects on the LAES spectrum.

Strong-field photoionization and detection of LAES spectra

We ionize the guest atom/molecule inside a droplet with femtosecond laser pulses from an amplified Ti:sapphire laser system (800 nm center wavelength, 25 fs pulse duration, 3 kHz repetition rate, 1 mJ maximum pulse energy), which we focus to obtain intensities of $I \leq 3 \cdot 10^{13} \frac{\text{W}}{\text{cm}^2}$, as indicated on top of Figures 1a-c. The pulse duration is measured with a single-shot autocorrelator and the intensity is calibrated using the U_P energy shift of electrons generated by ATI of H_2O at a pressure of $1 \cdot 10^{-7}$ mbar [36]. Laser-ionization of the doped droplets takes place inside the extraction region of a magnetic-bottle time-of-flight spectrometer and electron spectra are computed from flight-time measurements [28, 37]. We compare LAES spectra of atoms/molecules inside the droplets to ATI spectra of bare atoms/molecules, which we obtain as effusive beam from the pickup cell by blocking the He droplets. The measurement chamber is operated at a base pressure of 10^{-10} mbar.

3D scattering simulations

For the 3D scattering simulations, we assume an ensemble of electrons with a fixed kinetic energy E_{kin} . The ensemble with an isotropic distribution of initial directions propagates from the droplet center and scatters elastically until it finally exits the droplet. We assume binary electron-He collisions of mono-energetic electrons and neglect acceleration/deceleration due to LAES, as well as momentum transfer in elastic scattering events and inelastic interactions. The propagation distance before a scattering event, s is chosen from the exponential distribution $N(x) = N_0 \cdot e^{-n\sigma x}$ (Lambert-Beer law) as $s = -\frac{\log(R)}{(n\sigma)}$, with R uniformly distributed within the interval [0,1].

Values for the elastic scattering cross section σ and angular distribution $\frac{d\sigma}{d\Omega}$ are taken from Ref. [38] for electron energies up to 10 eV and from Ref. [39] for faster electrons. A constant He density of $n = 2.18 \cdot 10^{22} \frac{\text{Atoms}}{\text{cm}^3}$ [40] is assumed.

Data availability

The data measured, simulated, and analyzed in this study are available from the corresponding author on reasonable request.

Acknowledgements

We acknowledge financial support by the Austrian Science Fund (FWF) under Grants P 33166 and P 28475, as well as support from NAWI Graz.

Author contributions

M.K. conceived and designed the experiment with contributions of L.T. and M.K.-Z. ; P.H. built the experimental setup with contributions of B.T. and M.K.; L.T. B.T., and M.S. performed the experiment; L.T. performed the simulations with contributions of P.H.; L.T., B.T., M.K., and M.K.-Z. analyzed the data; all authors contributed to the interpretation of the results; L.T., and M.K. wrote the paper.

References

- [1] Krausz, F. & Ivanov, M. Attosecond physics. *Rev. Mod. Phys.* **81**, 163–234 (2009). URL <http://link.aps.org/doi/10.1103/RevModPhys.81.163>.
- [2] Smith, S. J. & Purcell, E. M. Visible Light from Localized Surface Charges Moving across a Grating. *Phys. Rev.* **92**, 1069–1069 (1953). URL <https://link.aps.org/doi/10.1103/PhysRev.92.1069>.
- [3] Jelley, J. V. *Cerenkov Radiation and Its Applications* (Creative Media Partners, LLC, 2018).

- [4] Compton, A. H. A Quantum Theory of the Scattering of X-rays by Light Elements. *Phys. Rev.* **21**, 483–502 (1923). URL <https://link.aps.org/doi/10.1103/PhysRev.21.483>.
- [5] Deacon, D. A. G. *et al.* First Operation of a Free-Electron Laser. *Phys. Rev. Lett.* **38**, 892–894 (1977). URL <https://link.aps.org/doi/10.1103/PhysRevLett.38.892>.
- [6] McPherson, A. *et al.* Studies of multiphoton production of vacuum-ultraviolet radiation in the rare gases. *J. Opt. Soc. Am. B* **4**, 595–601 (1987). URL <http://josab.osa.org/abstract.cfm?URI=josab-4-4-595>.
- [7] Corkum, P. B. & Krausz, F. Attosecond science. *Nat. Phys.* **3**, 381–387 (2007).
- [8] Spanner, M., Smirnova, O., Corkum, P. B. & Ivanov, M. Y. Reading diffraction images in strong field ionization of diatomic molecules. *J. Phys. B: At., Mol. Opt. Phys.* **37**, L243–L250 (2004). URL <https://doi.org/10.1088%2F0953-4075%2F37%2F12%2F102>.
- [9] Krüger, M., Schenk, M. & Hommelhoff, P. Attosecond control of electrons emitted from a nanoscale metal tip. *Nature* **475**, 78–81 (2011). URL <https://www.nature.com/articles/nature10196>.
- [10] Müller, M., Kravtsov, V., Paarmann, A., Raschke, M. B. & Ernstorfer, R. Nanofocused plasmon-driven sub-10 fs electron point source. *ACS Photonics* **3**, 611–619 (2016). URL <https://doi.org/10.1021/acsp Photonics.5b00710>.
- [11] Priebe, K. E. *et al.* Attosecond electron pulse trains and quantum state reconstruction in ultrafast transmission electron microscopy. *Nat. Photonics* **11**, 793–797 (2017). URL <https://doi.org/10.1038/s41566-017-0045-8>.
- [12] Morimoto, Y. & Baum, P. Diffraction and microscopy with attosecond electron pulse trains. *Nat. Phys.* **14**, 252–256 (2018). URL <https://doi.org/10.1038/s41567-017-0007-6>.
- [13] Siwick, B. J., Dwyer, J. R., Jordan, R. E. & Miller, R. J. D. An Atomic-Level View of Melting Using Femtosecond Electron Diffraction. *Science* **302**, 1382–1385 (2003). URL <https://science.sciencemag.org/content/302/5649/1382>.

- [14] Baum, P., Yang, D.-S. & Zewail, A. H. 4D Visualization of Transitional Structures in Phase Transformations by Electron Diffraction. *Science* **318**, 788–792 (2007). URL <https://science.sciencemag.org/content/318/5851/788>.
- [15] Barwick, B., Flannigan, D. J. & Zewail, A. H. Photon-induced near-field electron microscopy. *Nature* **462**, 902–906 (2009). URL <https://doi.org/10.1038/nature08662>.
- [16] Zewail, A. H. Four-dimensional electron microscopy. *Science* **328**, 187–193 (2010). URL <https://doi.org/10.1126/science.1166135>.
- [17] Gulde, M. *et al.* Ultrafast low-energy electron diffraction in transmission resolves polymer/graphene superstructure dynamics. *Science* **345**, 200–204 (2014). URL <https://science.sciencemag.org/content/345/6193/200>.
- [18] Hassan, M. T., Liu, H., Baskin, J. S. & Zewail, A. H. Photon gating in four-dimensional ultrafast electron microscopy. *Proceedings of the National Academy of Sciences* **112**, 12944–12949 (2015). URL <https://www.pnas.org/content/112/42/12944>.
- [19] Ryabov, A. & Baum, P. Electron microscopy of electromagnetic waveforms. *Science* **353**, 374–377 (2016). URL <https://science.sciencemag.org/content/353/6297/374>.
- [20] Kanya, R. & Yamanouchi, K. Femtosecond laser-assisted electron scattering for ultrafast dynamics of atoms and molecules. *Atoms* **7**, 85 (2019). URL <https://doi.org/10.3390/atoms7030085>.
- [21] Mason, N. J. Laser-assisted electron-atom collisions. *Rep. Prog. Phys.* **56**, 1275–1346 (1993). URL <https://doi.org/10.1088%2F0034-4885%2F56%2F10%2F002>.
- [22] Ehlotzky, F., Jaron, A. & Kaminski, J. Z. Electron-atom collisions in a laser field. *Phys. Rep.* **297**, 63–153 (1998). URL <http://www.sciencedirect.com/science/article/pii/S0370157397000756>.
- [23] Morimoto, Y., Kanya, R. & Yamanouchi, K. Laser-assisted electron diffraction for femtosecond molecular imaging. *J. Chem. Phys.* **140**, 064201 (2014). URL <https://doi.org/10.1063/1.4863985>.
- [24] Ghimire, S. *et al.* Observation of high-order harmonic generation in a bulk crystal. *Nat. Phys.* **7**, 138–141 (2010). URL <https://doi.org/10.1038/nphys1847>.

- [25] Toennies, J. P. & Vilesov, A. F. Superfluid helium droplets: A uniquely cold nanomatrix for molecules and molecular complexes. *Angew. Chem. Int. Ed.* **43**, 2622–2648 (2004). URL <https://doi.org/10.1002/anie.200300611>.
- [26] Callegari, C. & Ernst, W. E. Helium droplets as nanocryostats for molecular spectroscopy - from the vacuum ultraviolet to the microwave regime. In Merkt, F. & Quack, M. (eds.) *Handbook of High Resolution Spectroscopy* (John Wiley & Sons, Chichester, 2011).
- [27] Augst, S., Strickland, D., Meyerhofer, D. D., Chin, S. L. & Eberly, J. H. Tunneling ionization of noble gases in a high-intensity laser field. *Phys. Rev. Lett.* **63**, 2212–2215 (1989). URL <https://link.aps.org/doi/10.1103/PhysRevLett.63.2212>.
- [28] Thaler, B. *et al.* Femtosecond photoexcitation dynamics inside a quantum solvent. *Nat. Commun.* **9**, 4006 (2018). URL <https://doi.org/10.1038/s41467-018-06413-9>.
- [29] Brunger, M. J., Buckman, S. J., Allen, L. J., McCarthy, I. E. & Ratnavelu, K. Elastic electron scattering from helium: absolute experimental cross sections, theory and derived interaction potentials. *J. Phys. B: At., Mol. Opt. Phys.* **25**, 1823–1838 (1992). URL <https://doi.org/10.1088%2F0953-4075%2F25%2F8%2F016>.
- [30] Kroll, N. M. & Watson, K. M. Charged-particle scattering in the presence of a strong electromagnetic wave. *Phys. Rev. A* **8**, 804–809 (1973). URL <https://link.aps.org/doi/10.1103/PhysRevA.8.804>.
- [31] Kramida, A., Yu. Ralchenko, Reader, J. & and NIST ASD Team. NIST Atomic Spectra Database (ver. 5.8), [Online]. Available: <https://physics.nist.gov/asd> [2020, November 5]. National Institute of Standards and Technology, Gaithersburg, MD. (2020). URL <https://physics.nist.gov/asd>.
- [32] Tulsy, V. A., Krebs, B., Tiggesbäumker, J. & Bauer, D. Revealing laser-coherent electron features using phase-of-the-phase spectroscopy. *J. Phys. B: At., Mol. Opt. Phys.* **53**, 074001 (2020). URL <https://doi.org/10.1088%2F1361-6455%2Fab69ab>.
- [33] Thaler, B., Heim, P., Treiber, L. & Koch, M. Ultrafast photoinduced dynamics of single atoms solvated inside helium nanodroplets. *J. Chem. Phys.* **152**, 014307 (2020). URL <https://aip.scitation.org/doi/10.1063/1.5130145>.

- [34] Haberfehlner, G. *et al.* Formation of bimetallic clusters in superfluid helium nanodroplets analysed by atomic resolution electron tomography. *Nat. Commun.* **6**, 8779 (2015). URL <https://doi.org/10.1038/ncomms9779>.
- [35] Messner, R., Ernst, W. E. & Lackner, F. Shell-Isolated Au Nanoparticles Functionalized with Rhodamine B Fluorophores in Helium Nanodroplets. *J. Phys. Chem. Lett.* **12**, 145–150 (2020). URL <https://doi.org/10.1021/acs.jpcllett.0c03399>.
- [36] Boguslavskiy, A. E. *et al.* The multielectron ionization dynamics underlying attosecond strong-field spectroscopies. *Science* **335**, 1336–1340 (2012). URL <https://science.sciencemag.org/content/335/6074/1336>.
<https://science.sciencemag.org/content/335/6074/1336.full.pdf>.
- [37] Thaler, B. *et al.* Conservation of hot thermal spin–orbit population of ^2P atoms in a cold quantum fluid environment. *J. Phys. Chem. A* **123**, 3977–3984 (2019). URL <https://doi.org/10.1021/acs.jpca.9b02920>.
- [38] Dunseath, K. & Terao-Dunseath, M. Scattering of low-energy electrons by helium in a CO_2 laser field. *J. Phys. B: At., Mol. Opt. Phys.* **37**, 1305–1320 (2004). URL <https://doi.org/10.1088/0953-4075/37/6/013>.
- [39] The scattering cross sections taken from the data base provided by L. Bakaleinikov and A. Sokolov <http://www.ioffe.ru/ES/Elastic/>.
- [40] Harms, J., Toennies, J. P. & Dalfovo, F. Density of superfluid helium droplets. *Phys. Rev. B* **58**, 3341–3350 (1998). URL <https://link.aps.org/doi/10.1103/PhysRevB.58.3341>.